Materials Today Advances 6 (2020) 100030

Contents lists available at ScienceDirect

Materials Today Advances

journal homepage: www.journals.elsevier.com/materials-today-advances/

Forming indium-carbon (In—C) bonds at the edges of graphitic nanoplatelets

I.-Y. Jeon [a, b], S.-W. Kim [c], S.-H. Shin [c], S.-M. Jung [c], J.-B. Baek [c, *]

[a] Department of Chemical Engineering, Wonkwang University, 460, Iksandae-ro, Iksan, Jeonbuk, 54538, Republic of Korea
[b] Graphene Edge Co. Ltd., 460, Iksandae-ro, Iksan, Jeonbuk, 54538, Republic of Korea
[c] School of Energy and Chemical Engineering/Center for Dimension-Controllable Organic Frameworks, Ulsan National Institute of Science and Technology (UNIST), 50, UNIST, Ulsan, 44919, Republic of Korea

ARTICLE INFO

Article history:
Received 8 September 2019
Accepted 23 October 2019
Available online 6 February 2020

Keywords:
Indium
Graphitic nanoplatelets
Ball—milling
In—C bond formation
Oxygen reduction reaction

ABSTRACT

Indium (In), one of the soft and malleable post-transition metals, was introduced along the broken edges of graphitic nanoplatelets (GnPs) by mechanochemically ball-milling graphite in the presence of solid state In beads. After completely leaching off unreacted In using royal water (aqua regia), the formation of In—C bonds in the resulting In-doped graphitic nanoplatelets (InGnPs) was confirmed using various analytical techniques, including atomic-resolution transmission electron microscopy (AR-TEM). Scanning TEM (STEM) image shows that In elements instead of In clusters were uniformly distributed in the InGnPs, suggesting the formation of In—C bonds. The content of In in the InGnPs was 0.34 at% (3.01 wt%), as determined by X-ray photoelectron spectroscopy (XPS). The mechanochemically induced chemical reaction was powerful enough to form In—C bonds. Further, the InGnPs demonstrated catalytic activity toward the oxygen reduction reaction (ORR) comparable to commercial Pt/C catalysts, as well as excellent durability and tolerance against impurities (methanol and CO) in alkaline medium.

1. Introduction

Indium (In) is a member of the group 13 elements on the periodic table, with an electron configuration of $[Kr]4d^{10}5s^{2}5p^{1}$. It is a soft and malleable post-transition metal, and leaves a visible line on paper like a pencil lead, which is graphite. In is mostly used as a component in indium tin oxide (ITO) thin films and in transparent electrodes. Graphite, on the other hand, consists of a massive number of graphitic layers. Individual graphitic layers are called graphene, which are a unique example of an sp^2 carbon network with a two-dimensional (2D) honeycomb lattice. Graphene exhibits a wide range of important properties, including superior electrical conductivity [1], large surface area [2], excellent mechanical flexibility [3], and high thermal/chemical stability [4]. However, graphene is relatively inert and has poor dispersibility in solvents, which limits its applications. As a result, significant efforts have been devoted to the functionalization of graphene and graphitic nanoplatelets (<10 layers). Methods have used various functional groups containing different elements [5—7] such as boron (B) [8], nitrogen (N) [9], sulfur (S) [10], phosphorus (P) [11], antimony (Sb) [12], iodine (I) [13], selenium (Se) [14] and their mixtures [15,16]. The resulting array of functionalized graphene materials have been utilized in different applications, including flame retardants [17,18], energy conversion materials for the oxygen reduction reaction (ORR) [19], the cobalt reduction reaction (CRR) and iodine reduction reaction (IRR) [14], and energy storage materials for lithium (Li)-ion batteries [20,21]. To further expand the use of graphene materials, it would be highly useful to develop a simple method of forming In—C bonds. A facile method is essential for large scale production, which is necessary for commercial applications.

In this study, In—C bonds were formed along the broken edges of graphitic nanoplatelets (GnPs) by dry ball-milling graphite in the presence of In beads. This approach is based on the method for edge-selectively functionalized graphitic nanoplatelets (EFGnPs) *via* mechanochemical reaction [12,14,20—24]. The formation of In—C bonds was confirmed by atomic-resolution transmission electron microscopy (AR-TEM), which showed that the In bonded with GnPs at the element level, rather than in the form of In clusters. The resulting InGnPs was tested as an electrocatalyst for ORR, one of several potential applications. It showed competitive

* Corresponding author.
E-mail address: jbbaek@unist.ac.kr (J.-B. Baek).

https://doi.org/10.1016/j.mtadv.2019.100030

catalytic activity with excellent durability and tolerance against impurities (CO and methanol) in alkaline medium.

2. Experimental section

2.1. Materials

Graphite was obtained from Alfa Aesar (Natural, −100 mesh, 99.9995% metals basis) and used as received. Indium (beads, diam. 2−5 mm, 99.999% trace metals basis) was purchased from Aldrich Chemical Inc. and used as received. All other solvents were supplied by Aldrich Chemical Inc. and used without further purification, unless otherwise specified.

2.2. Preparation of InGnPs

The InGnPs was simply prepared using a ball milling approach. Graphite (5.0 g) and indium (5.0 g) were placed in a stainless steel container containing stainless steel balls (500 g, diameter 5 mm). After sealing, pressure was reduced to remove atmospheric air. The container was fixed on a planetary ball mill machine, then agitated at 500 rpm for 48 h. The resulting product was repeatedly washed with aqua regia to remove metallic impurities and any unreacted indium (or nitro-hydrochloric acid). Finally, it was freeze-dried at −120 °C under reduced pressure (0.05 mmHg) for 48 h to yield 5.89 g of dark black InGnPs powder (with an indium content of at least 0.89 g).

2.3. Instrumentation

Elemental analysis (EA) was conducted using a Thermo Scientific Flash 2000. The field emission scanning electron microscopy (FE-SEM) was performed on an FEI Nanonova 230. The high-resolution transmission electron microscopy (HR-TEM) was performed on a JEOL JEM-2100F microscope, and atomic resolution transmission electron microscopy (AR-TEM) was carried out on a Titan Cubed G2 60−300 microscope. The TEM specimens were prepared by dipping carbon microgrids (Ted Pella Inc., 200 Mesh Copper Grid) into well-dispersed samples in ethanol. Time-of-flight secondary ion mass spectrometry (TOF-SIMS) was carried out with a TOF-SIMS V instrument (ION-TOF GmbH, Germany) using a 10 keV Bi^+ primary ion beam source. The surface area was measured by nitrogen adsorption-desorption isotherms using the Brunauer−Emmett−Teller (BET) method on a Micromeritics ASAP 2504 N. X-ray photoelectron spectra (XPS) were recorded on a Thermo Fisher K-alpha XPS spectrometer. Thermogravimetric analysis (TGA) was conducted on a TA Q200 (TA Instrument) under air and nitrogen (N_2) at a heating rate of 10 °C/min. Micro-Raman measurements were made with a WiTec Alpha300S system with 532 nm wavelength laser light and a 50x objective. X-Ray diffraction (XRD) patterns were recorded with a Rigaku D/MAZX 2500V/PC with Cu−Kα radiation (35 kV, 20 mA, λ = 1.5418 Å). Zeta-potential values were determined using a Malvern Zetasizer (Nano ZS, Malvern Instruments).

2.4. Electrochemical measurements

The electrochemical tests were carried out using a computer-controlled potentiostat (1470E Cell Test System, Solartron Analytical, UK) and CompactStat.h as a bipotentiostat (Ivium Inc., NED) and RRDE-3A (ALS Co., Japan) with a typical three-electrode cell. Platinum mesh was used as a counter-electrode and an Ag/AgCl (Saturated KCl) electrode was used as a reference electrode. Briefly, InGnPs were dispersed in N,N-Dimethylformamide (DMF) and ultrasonicated for 5 min to form uniform catalyst inks (2 mg/mL). A total of 10 μL of a well-dispersed catalyst ink was loaded onto a glassy carbon (GC) disk electrode (5 mm in diameter) polished beforehand. After drying at room temperature, a Nafion (0.05 wt%) stock solution (1 μL) in ethanol was loaded onto the surface of the catalyst layer to form a thin protective film.

The cyclic voltammogram experiments were conducted in O_2- and N_2-saturated 0.1 M aq. potassium hydroxide (KOH) solution for ORR with various scan rates in the potential range from −0.9 V to 0.1 V at room temperature. Rotating disk electrode (RDE) measurements were performed in the O_2-saturated 0.1 M aq. KOH solution at a rotation speed varying from 600 to 2500 rpm and with a scan rate of 10 mV/s from −0.9 to 0.1 V. The detailed kinetic analysis was conducted according to Koutecky-Levich plots:

$$\frac{1}{j} = \frac{1}{j_k} + \frac{1}{B\omega^{0.5}} \quad (1)$$

where j_k is the kinetic current and B is the Levich slope:

$$B = 0.2nF(D_{O_2})^{2/3}\nu^{-1/6}C_{O_2} \quad (2)$$

Here n is the number of electrons transferred in the reduction of one O_2 molecule, F is the Faraday constant ($F = 96485$ C/mol), D_{O2} is the diffusion coefficient of O_2 ($D_{O2} = 1.9 \times 10^{-5}$ cm^2/s), ν is the kinematics viscosity for KOH ($\upsilon = 0.01$ cm^2/s) and C_{O2} is the concentration of O_2 in the solution ($C_{O2} = 1.2 \times 10^{-6}$ mol cm^{-3}). The constant 0.2 is adopted when the rotation speed is expressed in rpm. According to Equations (1) and (2), the number of electrons transferred (n) can be obtained from the slope of the Koutecky-Levich plot of i^{-1} vs. $\omega^{-1/2}$. From published data for F (96485 C mol^{-1}), D_{O2} (1.9×10^{-5} cm^2/s), vs. (0.01 cm^2/s), and C_{O2} (1.2×10^{-6} mol/ cm^3), B was calculated to be 0.144 mA/s$^{1/2}$ at $A = 0.19{,}625$ cm^2 for a four-electron exchange reaction ($n = 4$).

Rotating ring disk electrode (RRDE) experiments were carried out in an O_2-saturated 0.1 M aq. KOH solution. The potential was varied from 0.1 to −0.9 V at a potential sweep of 10 mV/s; the offset potential was set to 0.4 V (vs. Ag/AgCl). The four-electron selectivity of the catalyst was evaluated based on the H_2O_2 yield. The H_2O_2 yield and the electron transfer number (n) were determined using the following equations:

$$\%\,(H_2O_2) = 200 \times \frac{I_D/N}{I_D + I_R/N} \quad (3)$$

$$n = 4 \times \frac{I_D/N}{I_D + I_R/N} \quad (4)$$

where I_D is the disk current, I_R is the ring current, and N is the current collection efficiency of the Pt ring and is determined to be 0.424 [25,26].

The steady-state chronoamperometric response was tested at a polarizing potential of −0.3 V at 2500 rpm in O_2-saturated electrolyte by bubbling O_2 into the electrolyte. During this process, 3 M methanol (2.0 mL) or flow of CO gas was introduced into the electrolyte at 400 s to examine the methanol crossover and CO poisoning effect, respectively.

3. Results and discussion

As schematically presented in Fig. 1A and Fig. S1, the formation of In−C bonds was induced by a mechanochemical reaction, by dry ball milling graphite in the presence of In beads. To exclude the presence of free-standing In, the product InGnPs were repeatedly washed with aqua regia, and further with hydrochloric acid. Field-emission scanning electron microscopy (FE-SEM) images of the

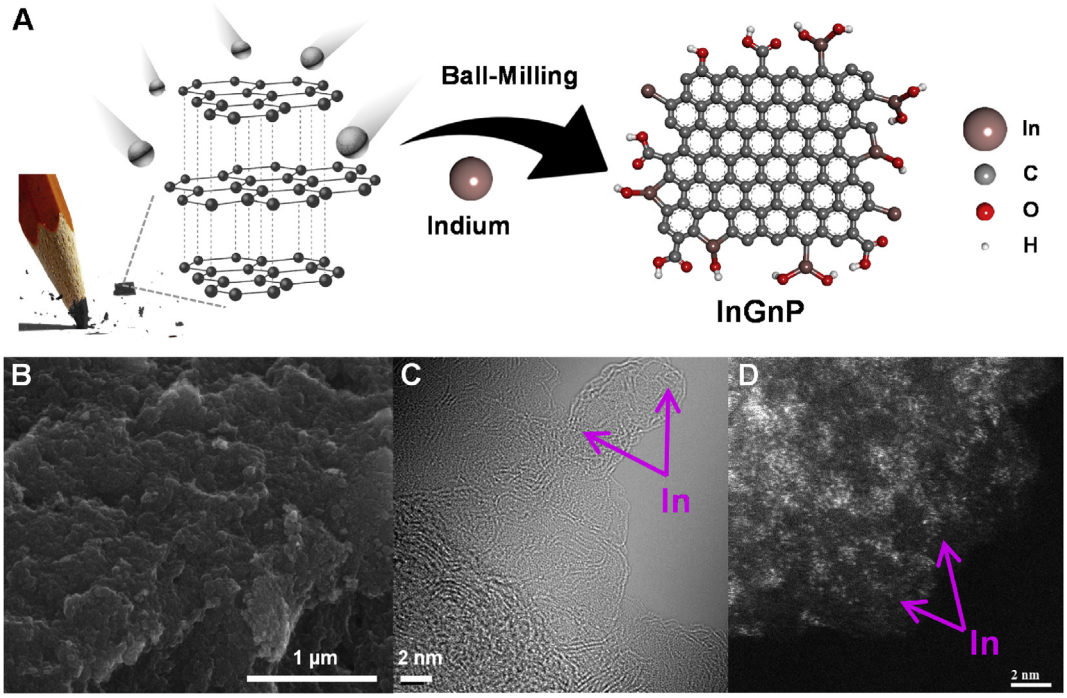

Fig. 1. (A) Schematic of indium (In)-doped graphitic nanoplatelets (InGnPs). (B) SEM image of InGnPs. (C) Atomic-resolution TEM (AR-TEM) image of InGnPs. (D) High-angle annular dark field (HAADF) scanning transmission electron microscopy (STEM) image of InGnPs.

pristine graphite showed a flake type morphology with large grain size (<150 μm) (Fig. S2). After ball milling and work up procedures, the grain size of the graphite was dramatically reduced to a few hundred nanometers (nm) (Fig. 1B and S3), indicating that unzipping of the graphitic C—C bonds had indeed occurred. Consequently, active carbon species emerged along the broken edges of the graphitic nanoplatelets (GnPs).

Similarly, In beads can also be cracked to produce active In species. Both carbon and In active species are required to form In—C bonds along the broken edges of the graphitic frameworks to yield InGnPs. SEM energy dispersive X-ray (EDX) spectra were obtained that showed the difference between the pristine graphite and InGnPs. The characteristic In peak together with C and O peaks were observed from the InGnPs, while only the C peak was observed from the pristine graphite (Fig. S4B). The corresponding element mapping images of C, O and In are presented in Fig. S4. The content of In determined using SEM EDX was 0.78 at% (6.76 wt%, Table S1).

To visually confirm the formation of In—C bonds in InGnPs, atomic-resolution transmission electron microscopy (AR-TEM) was utilized. At high magnification, the AR-TEM image of InGnPs shows dark dot contrasts along the edges that correspond to elemental In (pink arrows, black dots, Fig. 1C). High-resolution TEM (HR-TEM) images also show similar results (white arrows, Fig. S5). High-angle annular dark field (HAADF) scanning TEM (STEM) images from AR-TEM with atomic Z-contrast also confirmed that elemental In (pink arrows, Fig. 1D) was distributed at the atomic level, rather than nanoparticles and clusters. The result indicates that In—C bonds were formed by mechanochemical reaction as proposed in Fig. 1A. Once again, the HAADF STEM images from HR-TEM showed that In atoms were uniformly distributed on the indium-doped graphite nanoplatelets (InGnPs) without In clusters or other metallic particle debris (Fig. S6A-E).

Time-of-flight secondary ion mass spectrometry (TOF-SIMS) clearly confirmed the existence of indium (In) in the InGnPs. Typical positive ion mass spectra of the pristine graphite and InGnPs were obtained using a bismuth ion (Bi^+ ion) beam. The pristine graphite just showed various hydrocarbons peaks without related indium (isotopes $^{113}In^+$ and $^{115}In^+$), while the InGnPs spectra showed clear $^{113}In^+$ (m/z = 113) and $^{115}In^+$ (m/z = 115) peaks, isotopes of In (Fig. 2A and S7). The $^{115}In^+$ peak was sharper and higher intensity compared to the $^{113}In^+$ peak, because ^{115}In makes up to 95.7% of bulk indium [27].

We estimated the In content in the InGnPs using thermogravimetric analysis (TGA) in air because the boiling point of In is 2070 °C [28]. The char yield of the pristine graphite at 1,000 °C was 23.7 wt% (Fig. 2B and S8), due to the high thermal stability of the pristine, large grain size (<150 μm) graphite. However, the maximum weight loss of the InGnPs occurred at about 400 °C due to decomposition of the graphitic structure with small grain size (<1 μm), and oxygen-containing functional groups at the edges. Then, above 500 °C, the weight loss reached steady-state (6.9 wt%). Considering the char yields of other edge-selectively functionalized graphitic nanoplatelets (EFGnPs), which were about 0.0 wt% at 1,000 °C in air [22,29], the content of In_2O_3, which is the amphoteric oxide form of indium (In oxidizes in air at elevated temperature), was approximately 6.9 wt% at 1,000 °C (Fig. 2B). Hence, the actual content of In was about 5.56 wt%, which is consistent with the elemental analysis (EA) result (5.25 wt%, Table S1). The char yields of the pristine graphite and InGnPs at 1000 °C in N_2 were 99.1 and 80.5 wt%, respectively (Fig. S8). This means the difference (18.6 wt %) in weight loss between the pristine graphite and InGnPs is associated with various oxygenated functional groups (e.g. —COOH, —OH and —C=O) on the edges of the InGnPs.

X-ray photoelectron spectroscopy (XPS) was next utilized to investigate the elemental compositions of the materials. The pristine graphite showed a dominant C 1s peak with minor O 1s, which is attributed to physically adsorbed oxygen on the surface of the pristine graphite (Fig. 2C) [30]. InGnPs showed a clear characteristic In 3d peak along with C 1s and O 1s peaks as well as physically

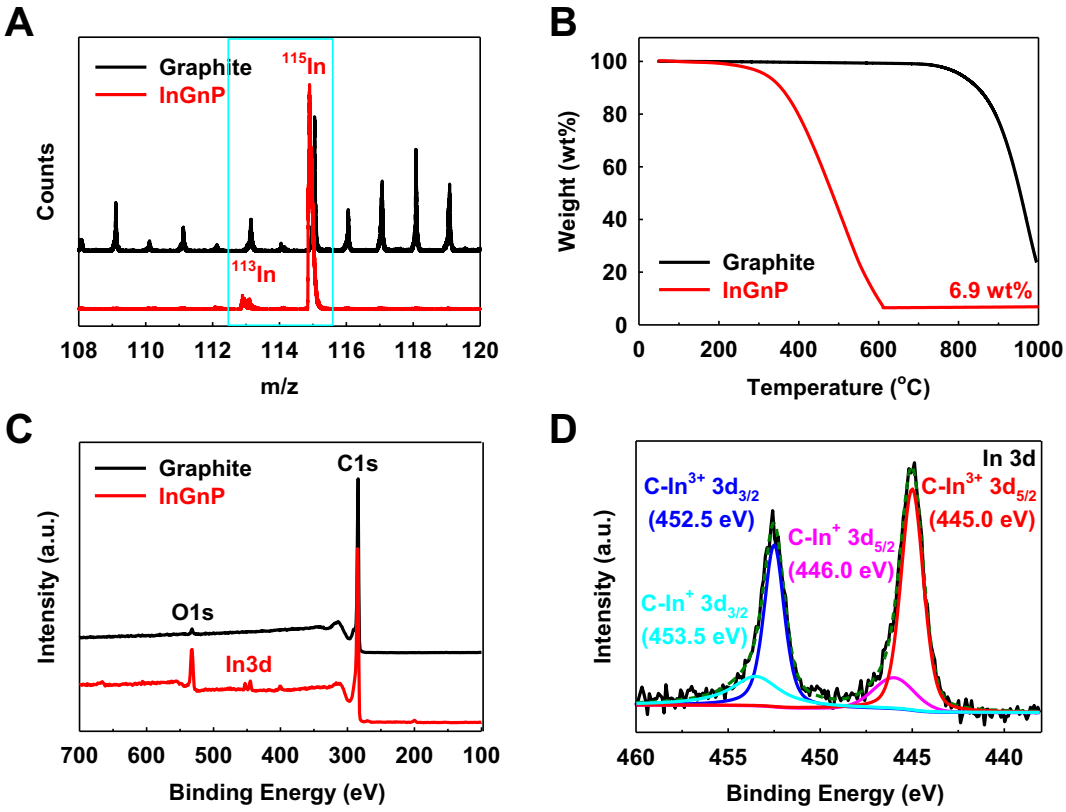

Fig. 2. (A) Time-of-flight secondary ion mass spectrometry (TOF-SIMS) spectra. (B) TGA thermograms obtained at the heating rate of 10 °C/min in air. (C) XPS full-scale survey spectra. (D) High-resolution XPS spectra of In 3d for InGnPs.

adsorbed N 1s and Cl 2p peaks. Besides, the indium content of the InGnPs was about 0.34 at% (3.01 wt%) (Table S1). In the high-resolution XPS spectra, the C 1s peak of InGnPs was classified into three components, sp^2 *C*–*C* (284.5 eV), *C*–O (285.7 eV) and *C*=O (288.5 eV), but the C–In peak did not appear, due to the overlap with the C–C peak and very low content of C–In bonds (Fig. S9A). The O 1s peak could be divided into two chemical bonds, C=*O* (531.6 eV) and C–*O* (533.3 eV) (Fig. S9B), because the remnant active carbon species were terminated with air/moisture (e.g.., O_2, CO_2 and H_2O) when the lid was opened.

In addition, the In 3d spectrum was divided into In $3d_{5/2}$ (445.0 eV) and In $3d_{3/2}$ (452.5 eV) peaks (Fig. 2D). Each peak was observed together with a shoulder peak, at 446.0 and 453.5 eV, respectively. The former two peaks at 445.0 and 452.5 eV were related to C–In^{3+} bonds [31]. The latter two peaks at 446.0 and 453.5 eV correspond to C–In^{+} bonds [32].

We can assume that the C–In^{+} ionic bonds at the edges of the InGnPs will provide excellent electrocatalytic activity for the oxygen reduction reaction (ORR) compared with C–In^{3+} ionic bonds, since indium (In) compounds are often powerful reducing agents [33,34].

The specific surface area was calculated using the Brunauer-Emmett-Teller (BET) plot of N_2 adsorption isotherms (Table S2). The pristine graphite showed a very low specific surface area (2.8 m^2/g) due to the highly ordered multilayered graphitic structure. However, after ball milling, the specific surface area (419.0 m^2/g) of the InGnPs increased 150 times compared to the pristine graphite, indicating that the graphite particles had significantly exfoliated into graphitic layers during the edge-selective In doping and delamination. Considering the maximum specific surface area (S_{BET} = 2630 m^2/g) of a single layer, the average number of layers in the InGnPs was calculated to be approximately 6.3 (2630/419 ≈ 6.3).

In addition, the InGnPs showed both type-I (P/P° = 0–0.5) and type-IV (P/P° = 0.5–1.0) isotherms, indicating the presence of micropores [35] and mesopores [36], respectively (Fig. S10A). The large surface area and co-existence of micropores and mesopores are likely to enhance the electrocatalytic activity of the InGnPs for ORR.

X-ray diffraction (XRD) patterns of the pristine graphite (Fig. S10B) showed strong [002], [004] and [006] peaks, which represent the direction perpendicular (*c*-axis) to the graphite hexagonal planes [37,38]. After ball milling, InGnPs showed only a [002] peak, shifted at 24.5° with very low intensity (only 0.2% of the pristine graphite), indicating that most of the graphite layers had delaminated into a few layers following the doping, lifting, and delaminating the edges of the InGnPs. This could have occurred because the atomic radius of In is 167 pm, which is approximately 2.3 times higher than carbon (70 pm) [39].

Raman spectroscopy is widely used to characterize carbon materials. The pristine graphite, a highly ordered graphite, has only a couple of Raman-active bands visible in the spectra. The in-phase vibration of the graphite lattice (G band) appears at 1585 cm^{-1} with a negligible disordered band (D band) (Fig. S10C). However, the G-band of InGnPs (1590 cm^{-1}) was shifted to a higher frequency (5 cm^{-1} blue-shift) due to phonon confinement caused by defects [40], which indicates the multilayered graphite crystal turned into a few graphitic layers [41] and the isolated double bonds resonate [42]. Furthermore, the InGnPs showed a high D-band intensity at 1345 cm^{-1} and a high I_D/I_G ratio (1.19), due to the increased contribution of the edge due to the decrease in grain size

(see Fig. 1B) and edge-distortion produced by In-doping (see Fig. 1C).

InGnPs were nicely dispersive in various solvents, including methanol, acetone, tetrahydrofuran (THF), *N*,*N*-dimethylacetamide (DMAc), *N*,*N*-dimethylformamide (DMF), *N*-methyl-2-pyrrolidone (NMP), and ethyl acetate (EAc) (Fig. S11). The good dispersibility allowed the InGnPs to be used in various applications.

Zeta-potential measurements were conducted to test the stability of the InGnP dispersion in NMP (Fig. S10D), and obtained values of −37.4 and −35.9 mV, respectively, at concentrations of 0.025 and 0.05 g/l. The results indicated the InGnPs were stably dispersed in NMP, because an absolute Zeta-potential over 30 mV signifies good dispersion stability [43].

The electrocatalytic activities of the InGnPs were measured by cyclic voltammograms (CV) in N_2 and O_2-saturated 0.1 M aq. KOH solutions, together with the pristine graphite and the commercial Pt/C catalysts as references (Fig. S12A-C). In contrast to the featureless CV curve in N_2-saturated condition, well-defined oxygen reduction peaks emerged in the O_2-saturated condition (Fig. 3A). The inflection points for the pristine graphite, the commercial Pt/C catalysts and InGnPs were located at −0.38, −0.22, and −0.22 V, respectively, with corresponding current densities of −0.16, −0.61 and −0.70 mA/cm^2. The current density of the InGnPs increased by 338% and 15% compared with the pristine graphite and the commercial Pt/C catalysts, respectively. This enhancement, compared to pristine graphite which is inert, indicates that In doping was responsible for the high electrocatalytic activity. More importantly, the cycle stability of the InGnPs was greatly superior to that of the pristine graphite and the commercial Pt/C catalysts (Fig. 3B and S12D-F). After 10,000 cycles in O_2-

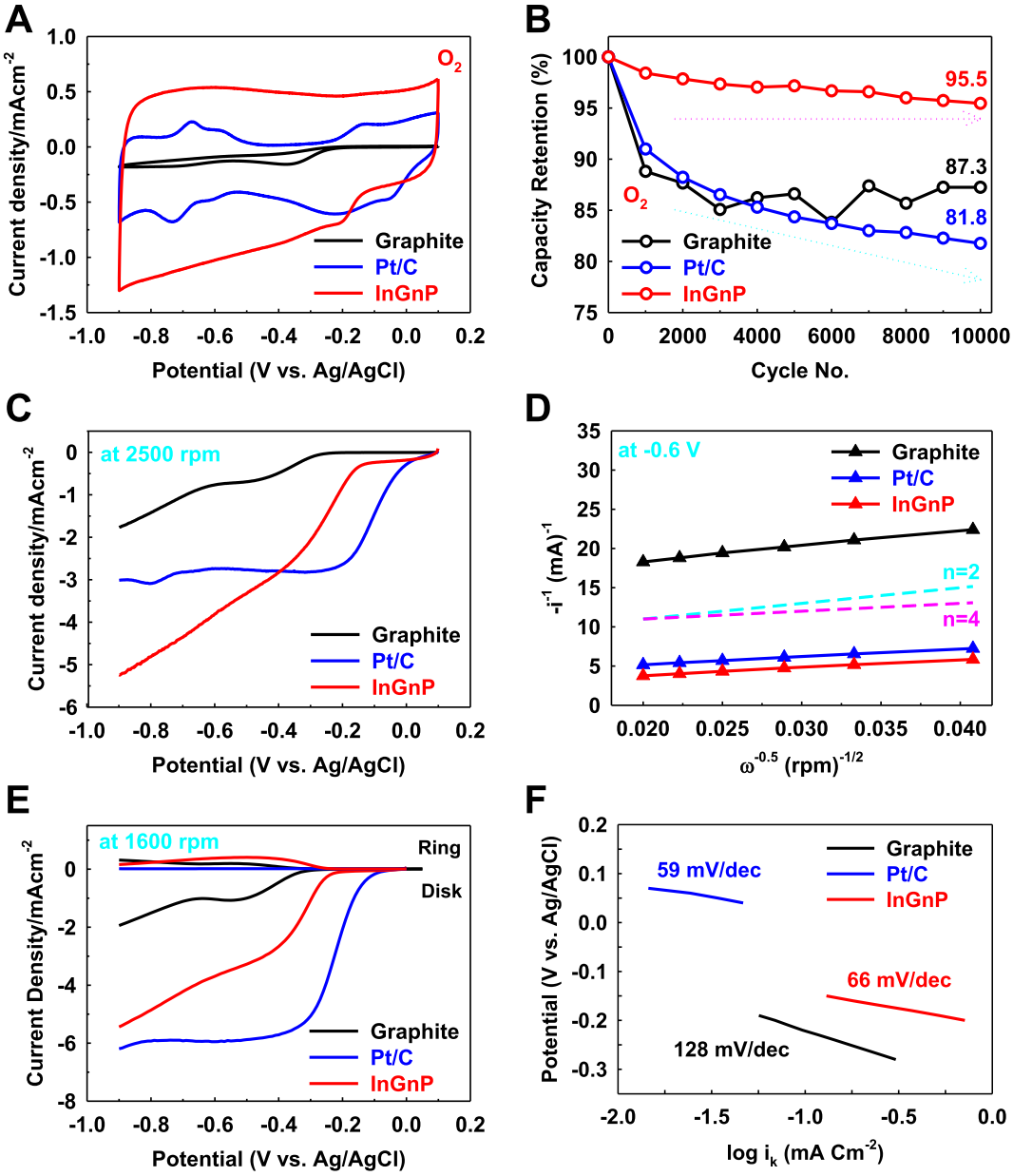

Fig. 3. Electrocatalytic activity of the pristine graphite, the commercial Pt/C catalysts and InGnPs for ORR: (A) Cyclic voltammograms in O_2-saturated 0.1 M aq. KOH solution with a scan rate of 10 mV/s. (B) Capacity retention in O_2-saturated 0.1 M aq. KOH solution with a scan rate of 100 mV/s. (C) Linear sweep voltammograms (LSV) at a rotation rate of 2500 rpm with a scan rate of 10 mV/s. (D) Koutecky-Levich plots derived from the RDE measurements at −0.6 V (vs. Ag/AgCl). (E) Rotating ring disk electrode (RRDE) linear sweep voltammograms at a rotation rate of 1600 rpm with a scan rate of 10 mV/s. (F) Tafel plots in O_2-saturated 0.1 M aq. KOH solution.

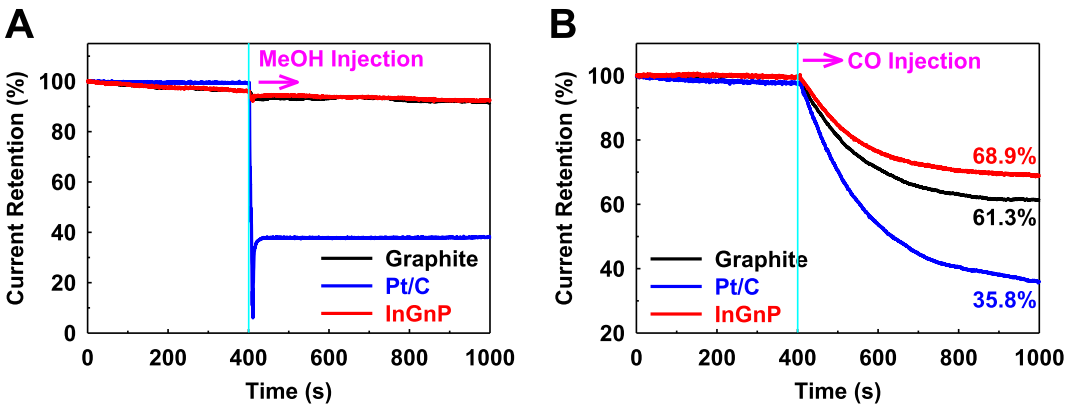

Fig. 4. The current time (*j*-*t*) chronoamperometric response at −0.3 V (vs. Ag/AgCl) and at a rotation rate of 2500 rpm: (a) 3 M methanol; (b) CO gas.

saturated 0.1 M aq. KOH solution at a scan rate of 100 mV/s, InGnPs showed only 4.5% capacitance loss, whereas the capacitances of the pristine graphite and the commercial Pt/C catalysts suffered substantial decreases of about 12.7% and 18.2%, respectively. Hence, the CV experiment indicates that In doping at the edges of the GnPs play a crucial role in improving ORR electrocatalytic activity and stability in alkaline medium.

To examine the electrochemical kinetics during the ORR process, rotating disk electrode (RDE) measurements were also performed in O_2-saturated 0.1 M aq. KOH solution at various rotating speeds and a constant scan rate of 10 mV/s (Fig. S13A-C). The oxygen reduction peak of the InGnPs was shifted more positively compared with the pristine graphite and showed a much higher limiting current density, −0.9 V, than both the pristine graphite and the commercial Pt/C catalysts (Fig. 3C). This result suggests that the In-doping reduced the ORR over-potential, thereby enhancing electrocatalytic activity.

The electron transfer number per oxygen molecule involved in the ORR was determined using the Koutecky-Levich equation, and found to be in the range of −0.4 ~ −0.6 V (Fig. S13D-F and Table S3, see details in the Experimental section) [44,45]. The experimentally determined n value of the pristine graphite at a potential of −0.6 V (Fig. 3D) was 2.0, indicating that the pristine graphite possessed a nearly two-step, classical two-electron process for ORR, with the production of a HO_2^- intermediate. On the other hand, the electron transfer number per O_2 molecule for the commercial Pt/C catalysts and the InGnPs was close to 4.0, indicating a one-step, four-electron reduction process, with the production of an OH^- intermediate.

To further investigate the electrocatalytic activity of the pristine graphite, the commercial Pt/C catalysts and InGnPs, rotating ring disk electrode (RRDE) measurements were performed in O_2-saturated 0.1 M aq. KOH solution at a rotation rate of 1600 rpm (Fig. 3E) [46,47]. The measured HO_2^- yields for the pristine graphite, the commercial Pt/C catalysts and InGnPs were 18.2−20.3%, 0.3−0.5% and 1.9−9.0%, respectively, in the potential range of −0.6 ~ −0.9 V (Fig. S14A). The corresponding electron transfer numbers were calculated to be 2.5, 4.0 and 3.1−3.8, respectively (Fig. S14B). This is consistent with the results obtained from the Koutecky-Levich plots based on RDE measurements, indicating that InGnPs proceeds mainly by a four-electron ORR mechanism.

Tafel slopes of the pristine graphite, the commercial Pt/C catalysts and InGnPs were 128, 59 and 66 mV/dec (decade being a unit for measuring frequency ratios on a logarithmic scale, with one decade corresponding to a ratio of 10 between two frequencies), respectively, in 0.1 M aq. KOH solution (Fig. 3F). The good ORR activity of the InGnPs was further confirmed by its much smaller Tafel slope compared with the pristine graphite, and comparable to the commercial Pt/C catalysts. The smaller Tafel slope corresponds to more favorable ORR kinetics, reconfirming the contribution of In-doping to the InGnPs' ORR activity.

The material's tolerance to impurities, such as methanol and carbon monoxide (CO), was evaluated by chronoamperometric responses after the addition of methanol or CO gas to the O_2-saturated 0.1 M aq. KOH solution at a rotation rate of 2500 rpm (Fig. 4). After adding 3 M methanol (2.0 mL), the current retentions for the pristine graphite and InGnPs did not show an obvious change, but the commercial Pt/C catalysts significantly decreased (Fig. 4A). After injecting CO gas, the current retentions for the pristine graphite and InGnPs similarly decreased to 61.3% and 68.9%, respectively, due to a decrease in O_2 concentration in the electrolyte by bubbling CO gas. However, at the same time, the current retention for the commercial Pt/C catalysts dramatically decreased to 35.8% (Fig. 4B), because of Pt poisoning caused by CO, in addition to the decrease in O_2 concentration in the electrolyte. The results obviously indicate that InGnPs has superior selectivity, long-term stability and tolerance against impurities, suggesting that InGnPs would be a good alternative to Pt-based ORR catalysts in alkaline media.

4. Conclusions

In summary, we carried out for the first time the formation of In−C bonds using a mechanochemical reaction between graphite and In beads in solid state. The formation In−C bonds in indium (In)-doped graphitic nanoplatelets (InGnPs) was confirmed using various analysis techniques including TEM, XPS, EDX, SEM, and TOF-SIMS. The results suggest that high-speed moving metal balls can deliver enough kinetic energy to generate active carbon and In species. The reaction between active carbon species and active In species resulted in the formation of In−C bonds at the edges of the InGnPs. The atomic level In-doping at the edges of the InGnPs led to highly enhanced electrocatalytic activity, excellent long-term stability and tolerance against methanol crossover and CO poisoning for the oxygen reduction reaction (ORR) compared with pristine graphite and commercial Pt/C catalysts. The results suggest that InGnPs is a potential alternative to commercial Pt/C catalysts in alkaline media.

Declaration of competing interest

The authors declare that they have no known competing financial interests or personal relationships that could have appeared to influence the work reported in this paper.

Acknowledgments

This research was supported by the Creative Research Initiative (CRI, 2014R1A3A2069102), BK21 Plus (10Z20130011057), the Science Research Center (SRC, 2016R1A5A1009405), and the Basic Science Research programs (2018R1D1A1B07041085) through the National Research Foundation (NRF) of Korea.

Appendix A. Supplementary data

Supplementary data to this article can be found online at https://doi.org/10.1016/j.mtadv.2019.100030.

References

[1] T.O. Wehling, K.S. Novoselov, S.V. Morozov, E.E. Vdovin, M.I. Katsnelson, A.K. Geim, A.I. Lichtenstein, Molecular doping of graphene, Nano Lett. 8 (1) (2008) 173–177.
[2] M.D. Stoller, S. Park, Y. Zhu, J. An, R.S. Ruoff, Graphene-based ultracapacitors, Nano Lett. 8 (10) (2008) 3498–3502.
[3] A. Fasolino, J.H. Los, M.I. Katsnelson, Intrinsic ripples in graphene, Nat. Mater. 6 (11) (2007) 858–861.
[4] A.A. Balandin, S. Ghosh, W. Bao, I. Calizo, D. Teweldebrhan, F. Miao, C.N. Lau, Superior thermal conductivity of single-layer graphene, Nano Lett. 8 (3) (2008) 902–907.
[5] Y. Xu, Z. Liu, X. Zhang, Y. Wang, J. Tian, Y. Huang, Y. Ma, X. Zhang, Y. Chen, A graphene hybrid material covalently functionalized with porphyrin: synthesis and optical limiting property, Adv. Mater. 21 (12) (2009) 1275–1279.
[6] Y. Xu, H. Bai, G. Lu, C. Li, G. Shi, Flexible graphene films via the filtration of water-soluble noncovalent functionalized graphene sheets, J. Am. Chem. Soc. 130 (18) (2008) 5856–5857.
[7] S. Stankovich, R.D. Piner, S.T. Nguyen, R.S. Ruoff, Synthesis and exfoliation of isocyanate-treated graphene oxide nanoplatelets, Carbon 44 (15) (2006) 3342–3347.
[8] T. Lin, F. Huang, J. Liang, Y. Wang, A facile preparation route for boron-doped graphene, and its CdTe solar cell application, Energy Environ. Sci. 4 (3) (2011) 862–865.
[9] L. Qu, Y. Liu, J.-B. Baek, L. Dai, Nitrogen-doped graphene as efficient metal-free electrocatalyst for oxygen reduction in fuel cells, ACS Nano 4 (3) (2010) 1321–1326.
[10] H.L. Poh, P. Šimek, Z. Sofer, M. Pumera, Sulfur-doped Graphene via Thermal exfoliation of graphite oxide in H_2S, SO_2, or CS_2 gas, ACS Nano 7 (6) (2013) 5262–5272.
[11] C. Zhang, N. Mahmood, H. Yin, F. Liu, Y. Hou, Synthesis of phosphorus-doped graphene and its multifunctional applications for oxygen reduction reaction and lithium ion batteries, Adv. Mater. 25 (35) (2013) 4932–4937.
[12] I.-Y. Jeon, M. Choi, H.-J. Choi, S.-M. Jung, M.-J. Kim, J.-M. Seo, S.-Y. Bae, S. Yoo, G. Kim, H.Y. Jeong, N. Park, J.-B. Baek, Antimony-doped graphene nanoplatelets, Nat. Commun. 6 (1) (2015).
[13] I.-Y. Jeon, H.-J. Choi, M. Choi, J.-M. Seo, S.-M. Jung, M.-J. Kim, S. Zhang, L. Zhang, Z. Xia, L. Dai, N. Park, J.-B. Baek, Facile, scalable synthesis of edge-halogenated graphene nanoplatelets as efficient metal-free eletrocatalysts for oxygen reduction reaction, Sci. Rep. 3 (2013) 1810.
[14] M.J. Ju, I.-Y. Jeon, H.M. Kim, J.I. Choi, S.-M. Jung, J.-M. Seo, I.T. Choi, S.H. Kang, H.S. Kim, M.J. Noh, J.-J. Lee, H.Y. Jeong, H.K. Kim, Y.-H. Kim, J.-B. Baek, Edge-selenated graphene nanoplatelets as durable metal-free catalysts for iodine reduction reaction in dye-sensitized solar cells, Sci. Adv. 2 (6) (2016) e1501459.
[15] Z.-S. Wu, A. Winter, L. Chen, Y. Sun, A. Turchanin, X. Feng, K. Müllen, Three-dimensional nitrogen and boron Co-doped graphene for high-performance all-solid-state supercapacitors, Adv. Mater. 24 (37) (2012) 5130–5135.
[16] S. Wang, L. Zhang, Z. Xia, A. Roy, D.W. Chang, J.-B. Baek, L. Dai, BCN graphene as efficient metal-free electrocatalyst for the oxygen reduction reaction, Angew. Chem. Int. Ed. 51 (17) (2012) 4209–4212.
[17] I.-Y. Jeon, S.-H. Shin, H.-J. Choi, S.-Y. Yu, S.-M. Jung, J.-B. Baek, Heavily aluminated graphene nanoplatelets as an efficient flame-retardant, Carbon 116 (2017) 77–83.
[18] M.-J. Kim, I.-Y. Jeon, J.-M. Seo, L. Dai, J.-B. Baek, Graphene phosphonic acid as an efficient flame retardant, ACS Nano 8 (3) (2014) 2820–2825.
[19] I.-Y. Jeon, D. Yu, S.-Y. Bae, H.-J. Choi, D.W. Chang, L. Dai, J.-B. Baek, formation of large-area nitrogen-doped graphene film prepared from simple solution casting of edge-selectively functionalized graphite and its electrocatalytic activity, Chem. Mater. 23 (17) (2011) 3987–3992.
[20] J. Xu, I.-Y. Jeon, H.-J. Choi, S.-J. Kim, S.-H. Shin, N. Park, L. Dai, J.-B. Baek, Metalated graphene nanoplatelets and their uses as anode materials for lithium-ion batteries, 2D Mater. 4 (1) (2016), 014002.
[21] I.-Y. Jeon, M.J. Ju, J. Xu, H.-J. Choi, J.-M. Seo, M.-J. Kim, I.T. Choi, H.M. Kim, J.C. Kim, J.-J. Lee, H.K. Liu, H.K. Kim, S. Dou, L. Dai, J.-B. Baek, Edge-fluorinated graphene nanoplatelets as high performance electrodes for dye-sensitized solar cells and lithium ion batteries, Adv. Funct. Mater. 25 (8) (2015) 1170–1179.
[22] I.-Y. Jeon, H.-J. Choi, S.-M. Jung, J.-M. Seo, M.-J. Kim, L. Dai, J.-B. Baek, Large-scale production of edge-selectively functionalized graphene nanoplatelets via ball milling and their use as metal-free electrocatalysts for oxygen reduction reaction, J. Am. Chem. Soc. 135 (4) (2012) 1386–1393.
[23] I.-Y. Jeon, H.-J. Choi, M.J. Ju, I.T. Choi, K. Lim, J. Ko, H.K. Kim, J.C. Kim, J.-J. Lee, D. Shin, S.-M. Jung, J.-M. Seo, M.-J. Kim, N. Park, L. Dai, J.-B. Baek, Direct nitrogen fixation at the edges of graphene nanoplatelets as efficient electrocatalysts for energy conversion, Sci. Rep. 3 (1) (2013).
[24] I.-Y. Jeon, S. Zhang, L. Zhang, H.-J. Choi, J.-M. Seo, Z. Xia, L. Dai, J.-B. Baek, Edge-selectively sulfurized graphene nanoplatelets as efficient metal-free electrocatalysts for oxygen reduction reaction: the electron spin effect, Adv. Mater. 25 (42) (2013) 6138–6145.
[25] D.-S. Yang, D. Bhattacharjya, M.Y. Song, J.-S. Yu, Highly efficient metal-free phosphorus-doped platelet ordered mesoporous carbon for electrocatalytic oxygen reduction, Carbon 67 (2014) 736–743.
[26] A. Byeon, J. Park, S. Baik, Y. Jung, J.W. Lee, Effects of boron oxidation state on electrocatalytic activity of carbons synthesized from CO_2, J. Mater. Chem. 3 (11) (2015) 5843–5849.
[27] J.R. de Laeter, J.K. Böhlke, P. De Bièvre, H. Hidaka, H.S. Peiser, K.J.R. Rosman, P.D.P. Taylor, Atomic weights of the elements. Review 2000 (IUPAC technical report), Pure Appl. Chem. 75 (6) (2003) 683–800.
[28] L.-W. Yin, Y. Bando, Y.-C. Zhu, D. Golberg, L.-W. Yin, M.-S. Li, Indium-assisted synthesis on GaN nanotubes, Appl. Phys. Lett. 84 (19) (2004) 3912–3914.
[29] I.-Y. Jeon, Y.-R. Shin, G.-J. Sohn, H.-J. Choi, S.-Y. Bae, J. Mahmood, S.-M. Jung, J.-M. Seo, M.-J. Kim, D. Wook Chang, L. Dai, J.-B. Baek, Edge-carboxylated graphene nanosheets via ball milling, Proc. Natl. Acad. Sci. 109 (15) (2012) 5588.
[30] A. Allouche, Y. Ferro, Dissociative adsorption of small molecules at vacancies on the graphite (0001) surface, Carbon 44 (15) (2006) 3320–3327.
[31] S.A. Webb, L. Baggetto, C.A. Bridges, G.M. Veith, The electrochemical reactions of pure indium with Li and Na: anomalous electrolyte decomposition, benefits of FEC additive, phase transitions and electrode performance, J. Power Sources 248 (2014) 1105–1117.
[32] V. Papaefthimiou, S. Kennou, The electronic structure of the sputtered indium–tin oxide and a thin conjugated oligomer film interface, Surf. Sci. 566–568 (2004) 497–501.
[33] N.N. Greenwood, A. Earnshaw, Chemistry of the Elements, Elsevier, Butherworkth-Heineman, Oxford, 1997, pp. 216–267.
[34] B.C. Ranu, P. Dutta, A. Sarkar, Indium as a reducing agent. Chemoselective reduction of α-halocarbonyl compounds and benzyl halides by indium metal in water under sonication, J. Chem. Soc. Perkin Trans. 1 (9) (1999) 1139–1140.
[35] M. Kruk, M. Jaroniec, K.P. Gadkaree, Nitrogen adsorption studies of novel synthetic active carbons, J. Colloid Interface Sci. 192 (1) (1997) 250–256.
[36] Y. Fang, D. Gu, Y. Zou, Z. Wu, F. Li, R. Che, Y. Deng, B. Tu, D. Zhao, A low-concentration hydrothermal synthesis of biocompatible ordered mesoporous carbon nanospheres with tunable and uniform size, Angew. Chem. Int. Ed. 49 (43) (2010) 7987–7991.
[37] M. Yoshio, H. Wang, K. Fukuda, Spherical carbon-coated natural graphite as a lithium-ion battery-anode material, Angew. Chem. Int. Ed. 42 (35) (2003) 4203–4206.
[38] M. Inagaki, K. Fujita, Y. Takeuchi, K. Oshida, H. Iwata, H. Konno, Formation of graphite crystals at 1000–1200°C from mixtures of vinyl polymers with metal oxides, Carbon 39 (6) (2001) 921–929.
[39] J.C. Slater, Atomic radii in crystals, J. Chem. Phys. 41 (10) (1964) 3199–3204.
[40] L.G. Cançado, M.A. Pimenta, B.R.A. Neves, M.S.S. Dantas, A. Jorio, Influence of the atomic structure on the Raman spectra of graphite edges, Phys. Rev. Lett. 93 (24) (2004).
[41] D. Graf, F. Molitor, K. Ensslin, C. Stampfer, A. Jungen, C. Hierold, L. Wirtz, Spatially resolved Raman spectroscopy of single- and few-layer graphene, Nano Lett. 7 (2) (2007) 238–242.
[42] K.N. Kudin, B. Ozbas, H.C. Schniepp, R.K. Prud'homme, I.A. Aksay, R. Car, Raman spectra of graphite oxide and functionalized graphene sheets, Nano Lett. 8 (1) (2008) 36–41.
[43] D.H. Everett, Basic Principles of Colloid Science, Royal Society of Chemistry, 2007, pp. 26–260.
[44] A.J. Bard, L.R. Faulkner, Electrochemical Methods: Fundamentals and Applications, second ed., Wiley, New York, 2001.
[45] Z.-W. Liu, F. Peng, H.-J. Wang, H. Yu, W.-X. Zheng, J. Yang, Phosphorus-doped graphite layers with high electrocatalytic activity for the O2 reduction in an alkaline medium, Angew. Chem. Int. Ed. 50 (14) (2011) 3257–3261.
[46] K. Gong, F. Du, Z. Xia, M. Durstock, L. Dai, Nitrogen-doped carbon nanotube Arrays with high electrocatalytic activity for oxygen reduction, Science 323 (5915) (2009) 760–764.
[47] Z.-S. Wu, S. Yang, Y. Sun, K. Parvez, X. Feng, K. Müllen, 3D nitrogen-doped graphene aerogel-supported Fe_3O_4 nanoparticles as efficient electrocatalysts for the oxygen reduction reaction, J. Am. Chem. Soc. 134 (22) (2012) 9082–9085.